Lasers in Manufacturing Conference 2019

A Genetic Algorithm for the Correlation of the Keyhole and the Melt Pool Depth in Laser Beam Welding of AA6082

Maximilian Schmoeller[a*], Maximilian Neureiter[a], Christian Stadter[a], Michael F. Zaeh[a]

[a]*Institute for Machine Tools and Industrial Management (iwb), Technical University of Munich, Boltzmannstr. 15, 85748 Garching, Germany*

Abstract

The aluminum alloy AA6082 is frequently used in high-voltage energy storage systems due to its favorable electrical and mechanical properties. Laser beam welding provides a flexible process for producing the welds. In order to protect the sensitive components of the battery cells, the required welding depth must be maintained. Optical Coherence Tomography (OCT) is a promising method for inline monitoring of the deep welding process. The measured depth of the keyhole can be used to set up a process control. A thermal simulation model was developed to take the difference between the melt pool depth and the keyhole depth into account. By adapting the keyhole geometry in the simulation based on genetic algorithms, a correlation was found through the optimization. The model was calibrated by comparing metallographic cross-sections with the computed melt pool geometries. Based on these results, a database can be created to improve the performance of the signal processing algorithms.

Keywords: FEM; Numerical Simulation; Deep Penetration Laser Beam Welding; Genetic Algorithm; Optical Coherence Tomography

1. Introduction

As a result of political developments, key industries such as the automotive and aviation industries are increasingly facing the challenges of lightweight construction. The demands for safety and quality of goods are increasing at the same time. One consequence of these developments is the need for new production processes that meet the diverse requirements of high-strength lightweight materials such as the aluminum alloy AA6082. Laser beam welding processes show great potential for joining these lightweight materials in terms of process efficiency, cycle time and flexibility. In order to enable the use of laser-based processes in series production, it is essential to ensure a high weld seam quality by means of inline process monitoring. Sensors based on Optical Coherence Tomography (OCT) can be used to observe the joining process and to

* Corresponding author. Tel.: +49-892-891-5492;
E-mail address: maximilian.schmoeller@iwb.mw.tum.de.

generate data from the process zone that is otherwise difficult to obtain. One parameter that can be reliably measured with OCT is the keyhole depth. This allows conclusions about the welding depth, which is an essential quality feature for many applications. However, there are difficulties in interpreting the keyhole depth measurement signal with regards to the welding depth, since a melt layer with a process-dependent thickness leads to an offset between the measurement and the target value. The presented approach aims at a calculation of the deviation between the measured keyhole depth and the weld seam depth using a numerical simulation model of the laser beam deep welding process. The obtained correlation is then used for the OCT data interpretation.

2. State of the Art

In this section, previous research work on numerical welding process simulation and a genetic optimization of heat source parameters is presented. HE 2012 and HE 2013 provided a comprehensive overview of the state of research on finite element (FE) analysis of laser-welded joints. Current research work on numerical process simulation in laser deep welding is supplemented in the following. XIA ET AL. 2014 used an FE model to predict the morphology of the melt pool cross-section. The results of the simulation were compared to experiments with an IPG YLS-4000 fiber laser using metallographic cross sections. By calculating the temperature field, XIA ET AL. 2014 were able to predict the size of the weld cross sections with a deviation of less than 8.9 %. SCHOBER 2014 developed a heat source calibration method for FE process simulation. This enabled the direct calculation of the heat source parameters based upon predefined reference data and without the need for a calibration using metallographic analysis methods. The approach is based on interpolation functions and the use of artificial neural networks. BELITZKI & ZAEH 2016 worked on the reduction of component distortions caused by laser beam welding. The manufacturing parameters were optimized by an FEM simulation. They developed a methodology for automated heat source calibration using optimization algorithms. They also investigated the applicability of Genetic Algorithms (GAs). For the laser hybrid welding of AA6082, FARAJI ET AL. 2015 developed a 3D heat source model considering effects within the keyhole which influence the energy input into the material. The coordinate system of the heat source was aligned so that a stationary vapor capillary in the finite volume model through the implementation of a relative movement of the workpiece was ensured. This modeling approach simplified the complex transient behavior to a quasi-stationary approach. Through the simulation, FARAJI ET AL. 2015 identified the Marangoni effect as the primary influencing effect on the flows within the melt pool. HAN ET AL. 2018 investigated the influence of reduced atmospheric pressure on the geometry of the melt pool and on pore formation. For this purpose, a comprehensive flow model for the AA5083 aluminum alloy was developed, in which laser beam reflections in the keyhole were also taken into account. In addition, a heat source was modeled which considers the damping and refraction of the laser radiation by the metal vapor escaping from the capillary. It was found that the reduced ambient pressure leads to a deepening of the keyhole. LIEBL ET AL. 2017 presented a numerical model for the calculation of the temperature field during laser welding with an adapted intensity distribution. In a 3D FE model, the fluid flow around a predefined keyhole geometry was calculated using temperature-dependent material properties. Both Marangoni convection and convection by metal vapor were considered. From the experimental results, regression models were developed which describe the characteristic dimensions of the melt pool. The numerical model was calibrated at the selected test points by adapting the melt isotherms to the cross-sections of the weld seams. The application of GAs for heat source calibration within an FEM simulation is a promising but rarely applied method.

3. Objectives and Approach

By using a finite element method simulation (FEM simulation), the relationship between the keyhole and the weld pool depth for laser beam deep penetration welding of AA6082 was investigated within the work described in this paper. It was intended to use this geometric quantity as a starting point for an evaluation algorithm of OCT keyhole measurements with regard to the welding depth and thus to increase the accuracy in the determination of the welding depth. The simulation model was based on the finite element method and was created using the simulation environment *Comsol Multiphysics 5.4*. The model calibration was performed by a GA, which was implemented with the *Matlab Global Optimization Toolbox*. The FE model is based on a numerical melt pool simulation according to LIEBL ET AL. 2017. It is used as part of the fitness function within the GA and therefore is solved several times in the iterative process, which is why computation time reducing modifications were necessary first. The model was then integrated into the GA. By an evolution-controlled variation of the geometric parameters of the modeled keyhole geometry, i.e. the heat source, two-dimensional projections of calculated melt pool envelopes were adapted to experimental cross sections. These originate from blind welding experiments with a multi-mode fiber laser. The GA results in an optimization cycle which minimizes the deviation of the simulated and experimental melt pool dimensions by adjusting the keyhole geometry in the model. The capillary geometry was modified by the

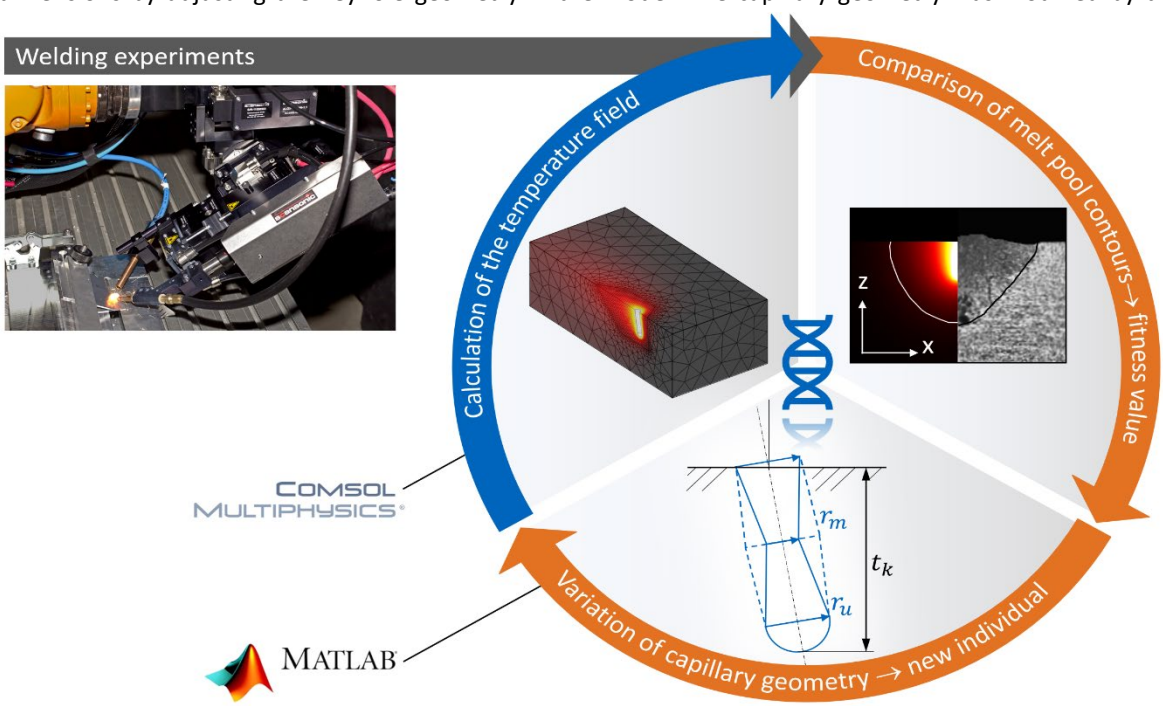

Fig. 1. Optimization process for the heat source geometry

capillary depth t_k, the radius in the capillary center r_m, and the radius of the capillary bottom r_u. Figure 1 shows the overall heat source optimization process by using a GA.

4. Methods and Experimental Setup

The heat source of the simulation is automatically calibrated by a computer-aided optimization algorithm, which is shown in Figure 2. By varying the geometry of the heat source (vapor capillary), the simulated melt pool shape, formed in the stationary condition, is adapted to the corresponding cross-section. After reaching a sufficient congruence, conclusions can be obtained about the real vapor capillary shape. Consequently, the deviation of the two melt pool contours represents the target function to be minimized. The following hyper parameters are specified to control the GA of the *Global Optimization Toolbox*:

- the population size p,
- the maximum number of generations g (termination criterion),
- a fitness limit f_{limit} (termination criterion),
- a number of elite individuals n_{elite},
- an upper and lower limit in the search space consisting of the keyhole parameters t_k, r_m and r_u, and
- the crossover ratio $p_{crossover}$.

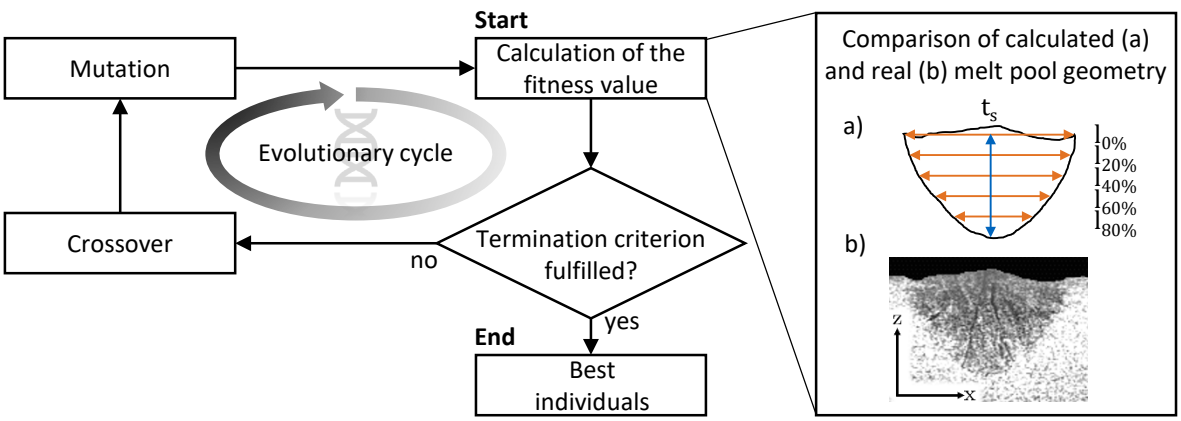

Fig. 2. Calculation sequence of the Genetic Algorithm

A GA developed by DEB ET AL. 2002 was adapted by WANG ET AL. 2013 in order to optimize the keyhole parameters. The algorithm is used for the maximization of *Derringer's desirability function*, which provides a conversion of all relevant measured variables y_i (width of the melt pool at discrete depths l_x and the depth of the melt pool t_s) into individual desirability functions d_i, where $0 \leq d_i \leq 1$ is the limit for the acceptable value range. The total desirability function D, which is to be maximized for m relevant variables, is calculated as

$$D = \prod_{i=1}^{m} (d_i)^{\frac{1}{m}}. \tag{1}$$

For the present case, the individual desirability functions d_i can be defined as:

$$d_i = \begin{cases} 0 & for\ y_i < L_i \\ \left(\frac{y_i - L_i}{T_i - L_i}\right)^w & for\ L_i \leq y_i \leq T_i \\ \left(\frac{U_i - y_i}{U_i - T_i}\right)^w & for\ T_i \leq y_i \leq U_i \\ 0 & for\ y_i > U_i \end{cases} \tag{2}$$

Here, L_i is the lower and U_i is the upper limit of the selected acceptable range and T_i is the target value. The variable w allows a weighting of individual desirability functions. The special importance of an accurate mapping of the melt pool depth t_s is reflected in the present optimization problem in the selection of the corresponding weight variable as $w_i = 2$. The fitness function $f(x)$ is defined as

$$f(x) = 1 - D(x), \tag{3}$$

where each individual is represented by the vector $x = (t_s, r_m, r_u)^T$. A value of $f(x) = 0$ corresponds to the alignment of both melt pool geometries in all lengths l_x and $f(x) = 1$ is assumed for deviations outside the accepted range.

Figure 3 shows a schematic representation of the experimental setup. An IPG YLR-8000 multimode fiber laser with a wavelength of 1070 nm, a fiber core diameter of $d_{c,M} = 200$ µm and a maximum output power of 8 kW was used for the experimental work. A Precitec YW52 fixed optics with an image ratio of 1:1.6 was employed for the beam guidance and focusing. This optical setup provided a focal diameter of $d_{f,M} = 320$ µm. The optics were manipulated by an industrial robot, which was also used to adjust the longitudinal angle of incidence α of the processing beam. A positive sign of the angle indicates a trailing process, while a negative sign indicates a leading process. The fixed optics were equipped with a Precitec IDM type OCT sensor system operating at a measuring rate of 70 kHz. The focus diameter of the measuring beam d_m was 50 µm. For further reference, SCHMÖLLER ET AL. 2019 provided a description of the measuring method and the influencing variables on the measurement of the keyhole depth.

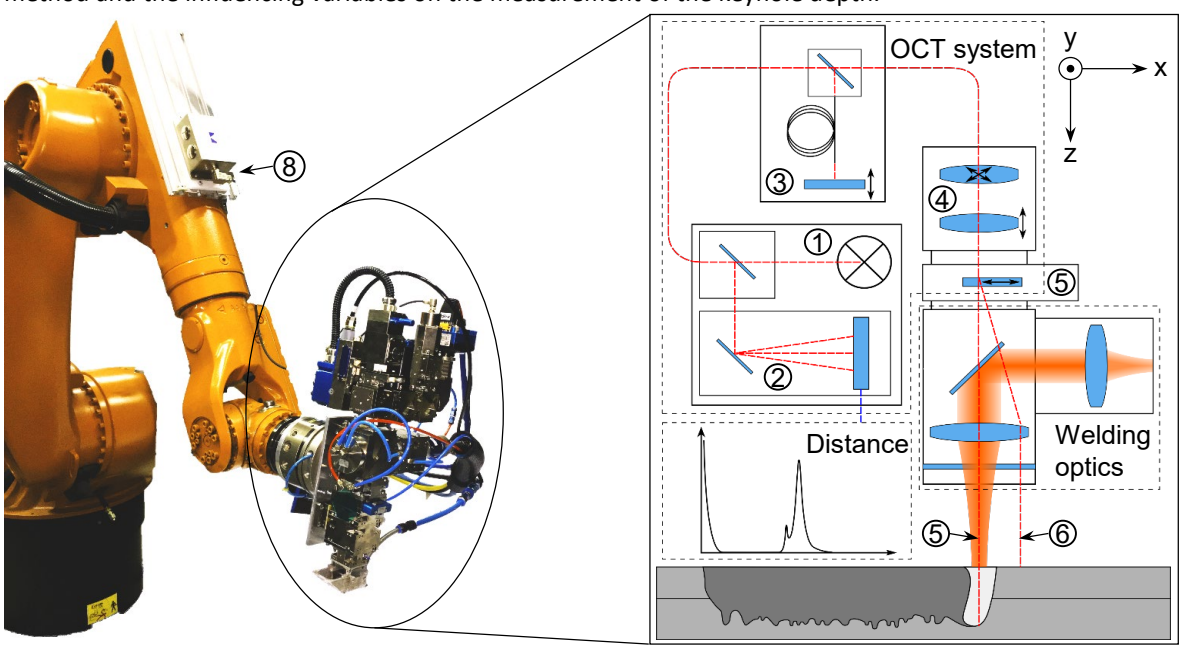

Fig. 3. Experimental setup

5. Numerical Model and Genetic Optimization

The following section describes the structure of the numerical simulation model. In this context, the implemented material properties, the initial model geometry, the meshing and the boundary conditions are discussed. For the analysis of the heat transfer within the fluid, the influences of pressure change and viscous dissipation are not considered. The following second order differential equation can be mathematically formulated as a form of energy conservation for stationary heat transfer:

$$\rho c_p \boldsymbol{v} \cdot \nabla T = \lambda_{th} \nabla^2 T + Q \qquad (4)$$

Here ∇ is the Nabla operator, ρ the mass density, c_p the specific isobaric heat capacity, $\boldsymbol{v}$ the velocity field of the fluid, T the temperature, λ_{th} the thermal conductivity and Q the introduced heat. The equation of fluid motion (Navier-Stokes equation) can be derived from a reformulation of the conservation of momentum. Under the neglect of volume forces, it can be described as

$$\rho(\boldsymbol{v} \cdot \nabla)\boldsymbol{v} = \nabla \cdot \left[-p\boldsymbol{I} + \mu_{dyn}(\nabla \boldsymbol{v} + (\nabla \boldsymbol{v})^T) - \frac{2}{3} \cdot \mu_{dyn}(\nabla \boldsymbol{v})\boldsymbol{I}\right] + F. \qquad (5)$$

Here $\boldsymbol{I}$ represents the unit tensor, p the pressure, μ_{dyn} the dynamic viscosity and F an external force. In order to solve the combined heat transport and flow problem, the equations 4 and 5 must be solved according to five variables v_x, v_y, v_z, p and T. For a solution of the dependent variables, information is obtained from a mass continuity equation:

$$\nabla \cdot (\rho \boldsymbol{v}) = 0 \qquad (6)$$

The Marangoni convection has a significant influence on the melt flow. This physical phenomenon occurs when the surface tension of an interface (generally liquid/gas) is temperature-dependent. The result is a shear stress, which is significantly affected by a tangential temperature gradient. The spatially focused energy input on the material surface induced by laser beam welding causes a high gradient of the temperature and consequently of the surface tension. Based on the Navier-Stokes equation, Marangoni convection for laminar flows can be described by the following relationship (RADAJ 1999, p. 101 and COMSOL 2018, p. 687):

$$\left[-p\boldsymbol{I} + \mu_{dyn}(\nabla \boldsymbol{v} + (\nabla \boldsymbol{v})^T) - \frac{2}{3} \cdot \mu_{dyn}(\nabla \boldsymbol{v})\boldsymbol{I}\right] \boldsymbol{n} = \frac{d\gamma}{dT} \cdot \nabla_t T \qquad (7)$$

The material properties are listed in Table 1. For the FEM simulation some material properties of the aluminum alloy AA6082 are modelled temperature dependent. As the numerical model of this work is based on a valid numerical model according to LIEBL ET AL. 2017, several of the material properties are adopted. The temperature-dependent material properties (see Table 2) were selected according to LIEBL ET AL. 2017. Due to a changed implementation of the phase transition in the FEM model, the characteristic values are defined for the solid and the liquid phases. The specific isobaric heat capacity c_p and the thermal conductivity λ_{th} are adopted unmodified from LIEBL ET AL. 2017. The dynamic viscosity μ_{dyn} and mass density ρ are approximated by linear correlations for an improvement of simulation convergence.

Table 1. Material properties of AA6082

Temperature-independent material properties			
Name	Symbol	Value	Unit
melting enthalpy	h_m	$390 \cdot 10^3$	J/kg
solidus temperature	T_s	848.15	K
melting temperature	T_m	885.65	K
liquidus temperature	T_l	923.15	K
evaporation temperature	T_v	2586.15	K
Surface tension at evaporation temperature	$\gamma \mid T_v$	0.3188	N/m
Temperature derivation of the surface tension	$-\mathrm{d}\gamma/\mathrm{d}T$	$-3.5 \cdot 10^{-4}$	N/(m · K)

Table 2. Temperature-dependent material properties of AA6082

Temperature-dependent material properties				
Name	Symbol	Value	solid liquid	Unit
dynamic viscosity	μ_{dyn}		500 0	Pa · s
density	ρ		$2750 - 0.18 \cdot \mathrm{T}$ $2656 - 0.30 \cdot \mathrm{T}$	kg/m^3
specific heat capacity	c_p	$\mathrm{h_m} \cdot \frac{\exp\left(-\frac{(\mathrm{T}-\mathrm{T_s})^2}{400}\right)}{20 \cdot \sqrt{\pi}} +$	$\begin{cases} 1170 \cdot \frac{\mathrm{T}}{\mathrm{T_m}} \\ 1170 \end{cases}$	J/(kg · K)
thermal conductivity	λ_{th}	$50 \cdot \left(1 - \tanh\frac{\mathrm{T}-\mathrm{T_m}}{15}\right) +$	$\begin{cases} 0.060 \cdot \mathrm{T} + 50 \\ 0.024 \cdot \mathrm{T} + 77 \end{cases}$	W/(m · K)

Figure 4 gives an overview of the boundary conditions and the geometric dimensions of the model geometry in the FEM simulation. Symmetry conditions for fluid mechanics and heat transport are defined on the sectional surface of the half model. The material flows with room temperature T_{amb} and feed velocity v_0 through the inlet in the y-direction. A pressure of $p = 0$ is defined on the outlet surface. The remaining

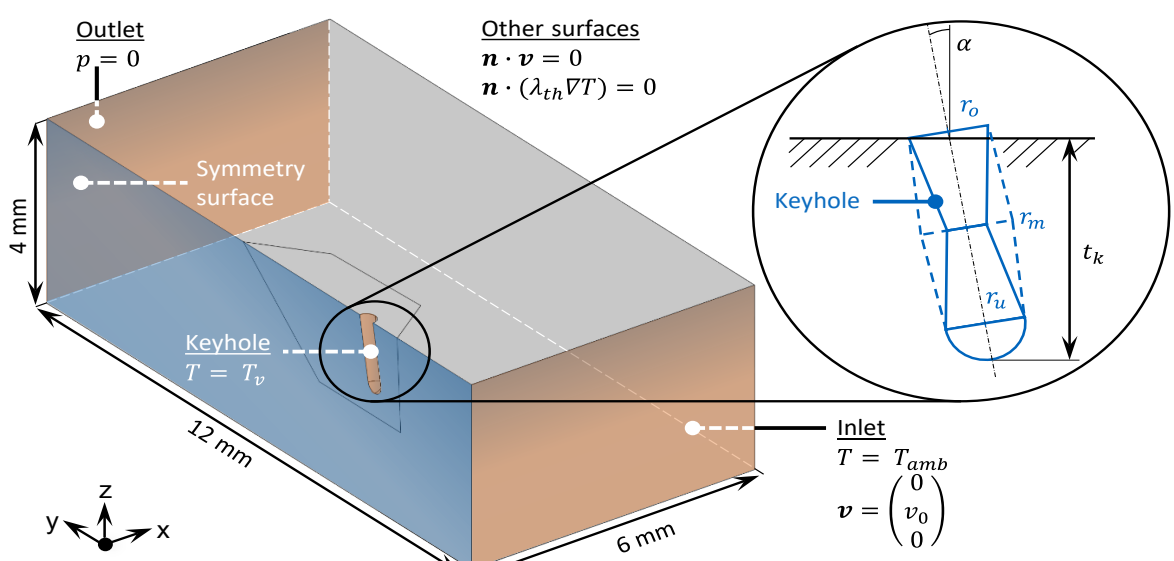

Fig. 4. Geometric dimensions and boundary conditions of the numerical simulation model

surfaces are assumed to be rigid, adiabatic walls limiting the flow and heat transfer: $\boldsymbol{n} \cdot \boldsymbol{v} = 0$ and $\boldsymbol{n} \cdot (\lambda_{\mathrm{th}} \nabla T) = 0$. Here $\boldsymbol{n}$ is the normal vector. On the interface between the liquid melt pool and the vapor capillary, the evaporation temperature T_v of the alloy AA6082 is uniformly applied over the entire surface.
The geometry of the numerical model is meshed with tetrahedral volume elements (see Figure 5). Two areas with different mesh parameters can be distinguished: The hexahedron-shaped area around the vapor capillary shows a finer mesh, since the geometric shape of the melt pool is of primary interest. For the remaining area, a coarser mesh could be selected in order to reduce the computing time. Depending on the size of the vapor capillary, the dimension of the finely meshed area was adjusted. A consistently high quality of the mesh elements is thus ensured. The mesh parameters can be found in Table 3.

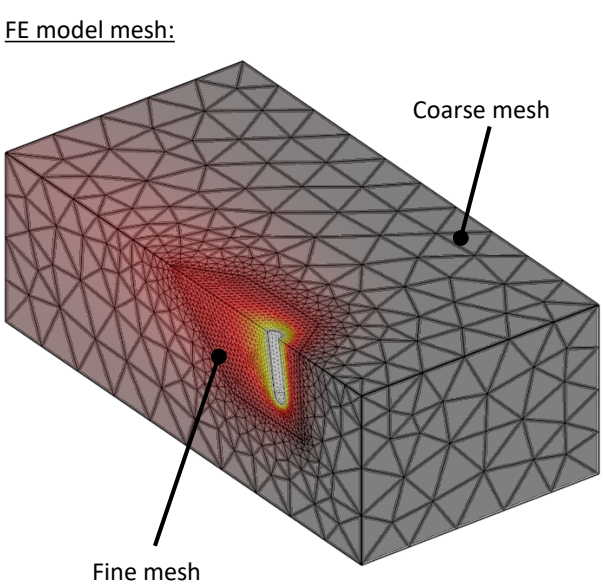

Geometry 1

$t_s = 0.5$ mm
$r_m = 185$ µm
$r_u = 135$ µm

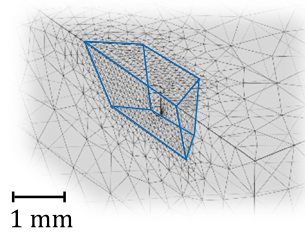

Number of elements	20900
Average element quality	0.6618

Geometry 2

$t_s = 1.0$ mm
$r_m = 185$ µm
$r_u = 135$ µm

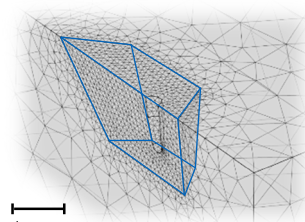

Number of elements	34800
Average element quality	0.6618

Fig. 5. Meshing of the model geometry and examples for varying vapor capillary dimensions

Table 3. Mesh parameters of the numerical model

Mesh parameter	Fine mesh	Coarse mesh
Max. element size	0.12 mm	1.60 mm
Max. growth rate	7 %	50 %

6. Results and discussion

In the following, the results of an exemplary heat source calibration of the finite element method model (FEM model) using the Genetic Algorithm (GA) are presented. Derringer's desirability function D was parameterized with the variables of the individual desirability functions defined in Table 4. Figure 6 (left) shows an example of individual fitness over all generation steps of the optimization process. While the fitness of generation 0 is predominantly outside the accepted range (individuals with $f(x) = 1$), a trend towards better values is discernible with advancing generations. An improvement of $f(x)$ essentially takes place in the first five to six generations. Optimizations with far more generations ($g = 20$) showed no significant further improvements in later generations. The result of an exemplary GA optimization is shown in Figure 6 (right) as a superposition of the simulated melt pool with the cross-section. The final capillary geometry (blue) of the GA development leads to a molten bath shape (orange), which simulates the considered support points in the defined depths (white crosses) of the micrograph best. While the melt pool contour of the cross section was well reproduced by the simulation, slight deviations at the upper two and the lowest support point are noticeable. These result from a small number of geometric degrees of freedom of the capillary shape. It can be assumed that the implementation of further variable keyhole radii leads to an improvement in this respect. The additional degrees of freedom could allow the representation of more differentiated melt pool shapes and thus a better adaptation. A suitable validation method is required to apply the model. Therefore, different possibilities for validation were considered, whereby the corresponding experiments still have to be carried out. Once the validation has been completed, the model can be used for database generation.

Table 4. Hyperparameters for the genetic optimization of the keyhole geometry

i	$y_i(x)$	T_i	L_i	U_i	w_i
1	$t_{s,Sim}(x)$	t_s	$0.6 \cdot t_s$	$1.4 \cdot t_s$	2
2	$l_{0\%,Sim}(x)$	$l_{0\%}$	$0.6 \cdot l_{0\%}$	$1.4 \cdot l_{0\%}$	1
3	$l_{20\%,Sim}(x)$	$l_{20\%}$	$0.6 \cdot l_{20\%}$	$1.4 \cdot l_{20\%}$	1
4	$l_{40\%,Sim}(x)$	$l_{40\%}$	$0.6 \cdot l_{40\%}$	$1.4 \cdot l_{40\%}$	1
5	$l_{60\%,Sim}(x)$	$l_{60\%}$	$0.6 \cdot l_{60\%}$	$1.4 \cdot l_{60\%}$	1
6	$l_{80\%,Sim}(x)$	$l_{80\%}$	$0.6 \cdot l_{80\%}$	$1.4 \cdot l_{80\%}$	1

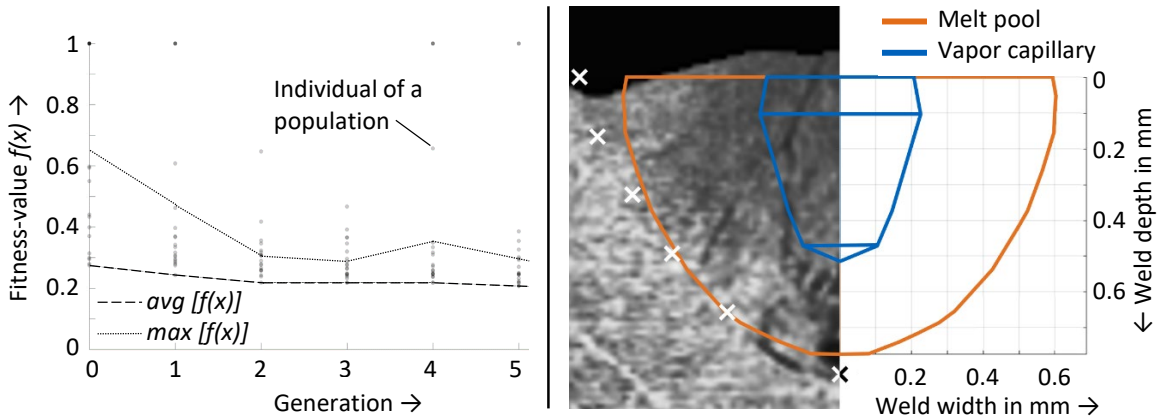

Fig. 6. Optimized keyhole geometry ($P_{FL} = 3{,}9\ kW, v_w = 10\frac{m}{min}, \alpha = -10°$)

Acknowledgments

The results presented were developed within the project RoKtoLas, which is funded from the German Federal Ministry of Education and Research (BMBF) within the funding program Photonics Research Germany (contract number 13N14555) and supervised by the VDI Technology Centre (VDI TZ). We thank the BMBF and the VDI TZ for their support and the good and trustful cooperation.

References

BELITZKI & ZAEH 2016
Belitzki, A.; Zaeh, M. F.: Accuracy of calculated component distortions using the weld pool length to calibrate the heat source. Journal of Laser Applications 28 (2016) 2, p. 22424.
COMSOL 2018
Comsol: The Heat Transfer Module User's Guide. 2018.
DEB ET AL. 2002
Deb, K.; Pratap, A.; Agarwal, S.; Meyarivan, T.: A fast and elitist multiobjective genetic algorithm. NSGA-II. IEEE Transactions on Evolutionary Computation 6 (2002) 2, pp. 182 – 197.
FARAJI ET AL. 2015
Faraji, A. H.; Goodarzi, M.; Seyedein, S. H.; Barbieri, G.; Maletta, C.: Numerical modeling of heat transfer and fluid flow in hybrid laser–TIG welding of aluminum alloy AA6082. The International Journal of Advanced Manufacturing Technology 77 (2015) 9-12, pp. 2067 – 2082.
HAN ET AL. 2018
Han, X.; Tang, X.; Wang, T.; Shao, C.; Lu, F.; Cui, H.: Role of ambient pressure in keyhole dynamics based on beam transmission path method for laser welding on Al alloy. The International Journal of Advanced Manufacturing Technology 99 (2018) 5-8, pp. 1639 – 1651.
HE 2012
He, X.: Finite Element Analysis of Laser Welding: A State of Art Review. Materials and Manufacturing Processes 27 (2012) 12, pp. 1354 – 1365.
HE 2013
He, X.: Numerical Studies on Laser Welding Process. Applied Mechanics and Materials 440 (2013), pp. 158 – 164.
LIEBL ET AL. 2017
Liebl, S.; Stadter, C.; Ganser, A.; Zaeh, M. F.: Numerical simulation of laser beam welding using an adapted intensity distribution. Journal of Laser Applications 29 (2017) 2, p. 22405.
RADAJ 1999
Radaj, D.: Schweißprozeßsimulation. Grundlagen und Anwendungen. Düsseldorf: Verl. für Schweißen und verwandte Verfahren DVS-Verl. 1999. ISBN: 3-87155-188-0. (Fachbuchreihe Schweißtechnik 141).
SCHMÖLLER ET AL. 2019
Schmöller, M.; Stadter, C.; Liebl, S.; Zaeh, M. F.: Inline Weld Depth measurement for High brilliance Laser Beam Sources Using Optical

Coherence Tomography. Journal of Laser Applications 31 (2019) 2, p. 22409.
SCHOBER 2014
Schober, A.: Eine Methode zur Wärmequellenkalibrierung in der Schweißstruktursimulation. München: Herbert Utz Verlag GmbH 2014. ISBN: 9783831644155. (Forschungsberichte IWB 291).
WANG ET AL. 2013
Wang, X.; Chen, H.; Liu, H.; Li, P.; Yan, Z.; Huang, C.; Zhao, Z.; Gu, Y.: Simulation and optimization of continuous laser transmission welding between PET and titanium through FEM, RSM, GA and experiments. Optics and Lasers in Engineering 51 (2013) 11, pp. 1245 – 1254.
XIA ET AL. 2014
Xia, P.; Yan, F.; Kong, F.; Wang, C.; Liu, J.; Hu, X.; Pang, S.: Prediction of weld shape for fiber laser keyhole welding based on finite element analysis. The International Journal of Advanced Manufacturing Technology 75 (2014) 1-4, pp. 363 – 372.